Incompatibility of argon during magma ocean crystallization

Colin R.M. Jackson [a],[*], Curtis D. Williams [b], Zhixue Du [c], Neil R. Bennett [d], Sujoy Mukhopadhyay [b], Yingwei Fei [e]

[a] Department of Earth and Environmental Sciences, Tulane University, USA
[b] Earth and Planetary Sciences Department, University of California, Davis, USA
[c] State Key Laboratory of Isotope Geochemistry, Guangzhou Institute of Geochemistry, Chinese Academy of Sciences, Guangzhou, China
[d] Department of Chemistry and Biochemisry, California State University, East Bay, USA
[e] Earth and Planets Laboratory, Carnegie Institution for Science, USA

ARTICLE INFO

ABSTRACT

We report results from multi-anvil (MA) and laser-heated diamond anvil cell (LH-DAC) experiments that synthesize high-pressure phases, including bridgmanite, ferropericlase, stishovite, and ultramafic liquid, in the presence of an argon-rich fluid. The goal of the experiments is to constrain the equilibrium distribution of argon in magma ocean environments. Argon concentrations in LH-DAC experiments were quantified by electron microprobe analysis, while argon concentrations in MA experiments were quantified by laser-ablation mass spectrometry and electron microprobe analysis. Our LH-DAC experiments demonstrate that argon solubility in ultramafic liquid is near or above 1.5 wt.% at conditions between 13–101 GPa and 2300–6300 K. Argon concentrations in bridgmanite and ferropericlase synthesized in LH-DAC experiments range from below detection to 0.58 wt.%. Argon concentrations in bridgmanite and ferropericlase synthesized in MA experiments range from below detection to 2.16 wt.% for electron microprobe measurements and laser-ablation measurements. We interpret this wide range of argon concentrations in minerals to reflect the variable presence of argon-rich fluid inclusions in analytical volumes. Our analyses therefore provide upper limit constraints for argon solubility in high-pressure minerals (<0.015 wt.%) across all mantle pressures and temperatures. The combination of relatively high argon solubility in ultramafic liquid (~1.5 wt.%) and low argon solubility in minerals implies argon incompatibility ($D^{Ar}_{bridgmanite-melt} < 0.01$, $D^{Ar}_{ferropericlase-melt} < 0.01$) during magma ocean crystallization and that the initial distribution of argon, and likely other neutral species, may be controlled by liquids trapped in a crystallizing magma ocean. We thus predict a basal magma ocean would be enriched in noble gases relative to other regions of the mantle. Moreover, we predict that the noble gas parent-daughter ratio of magma ocean cumulates pile will increase with crystallization, assuming refractory and incompatible behavior for parent elements.

© 2020 Elsevier B.V. All rights reserved.

1. Introduction

Ocean island basalts contain materials that were isolated from the convective mantle extremely early in solar system history and have remained geochemically distinct to the modern day (Mukhopadhyay, 2012; Peto et al., 2013; Caracausi et al., 2016; Rizo et al., 2016; Mundl et al., 2017; Williams and Mukhopadhyay, 2019). Evidence for early-isolated or primordial mantle materials largely comes from studies of W isotopes and the noble gases, including helium (He), neon (Ne), argon (Ar), krypton (Kr) and xenon (Xe). Noble gases are uniquely suited to trace Earth's earliest his-

tory because they are a group of highly atmophile, largely inert elements (Brooker et al., 2003; Heber et al., 2007; Jackson et al., 2013; Graham et al., 2016). Furthermore, the group is rich in radiogenic isotopes, produced from both short- and long-lived decay systems. Indeed, it was the observation of a high ^{3}He/^{4}He component within intraplate magmas that first suggested the mantle contains a primordial, less degassed geochemical component (Jenkins, 1978; Kaneoka and Takaoka, 1980; Kurz et al., 1982). This view of the mantle has been reinforced by continued analyses of Ne and Ar isotopes produced by radio-decay (Honda et al., 1991; Farley and Craig, 1994; Burnard et al., 1997; Trieloff et al., 2000; Moreira et al., 2001; Kurz et al., 2009).

More recently, Xe isotopes now constrain the formation of high ^{3}He/^{4}He materials to within the lifetime of ^{129}I, or within the first 80 Ma of solar system history (Mukhopadhyay, 2012; Peto et al.,

* Corresponding author.
E-mail address: cjackson2@tulane.edu (C.R.M. Jackson).

2013; Caracausi et al., 2016). A separate timing constraint is gained from the discovery of Ne derived from the solar nebula in high ^{3}He/^{4}He materials (Williams and Mukhopadhyay, 2019), as solar nebular gases were dissipated from the solar system within the first 10 Ma of solar system history (e.g., Mamajek, 2009). These timing constraints combine to indicate that high ^{3}He/^{4}He materials were first isolated during the era of accretion. This is the time when magma ocean formation and crystallization was a dominant mechanism for mass transfer within terrestrial planets.

In this contribution we focus on the partitioning behavior of Ar during magma ocean solidification in order to constrain the initial distribution of noble gases within the mantle-atmosphere system. Strong partitioning of Ar into mineral phases would lead to the sequestration of large amounts of Ar into Earth's primordial mantle, leaving an Ar-poor atmosphere in response. Partitioning behavior can be quantified as either the equilibrium concentration or solubility ratio of Ar in two phases ($D^{Ar}_{min-melt} = \frac{[Ar]_{mineral}}{[Ar]_{melt}} = \frac{Sol.^{Ar}_{mineral}}{Sol.^{Ar}_{melt}}$).

The large majority of experimental and observational data indicate that Ar and other noble gases are extremely incompatible ($D^{noble\ gas}_{min-melt} < 10^{-3}$) within the uppermost mantle (<3 GPa) (Chamorro et al., 2002; Brooker et al., 2003; Heber et al., 2007; Delon et al., 2019; Jackson et al., 2013; Graham et al., 2016). Although Watson et al. (2007) report high Ar solubility in olivine and pyroxene at low Ar fugacity (fAr). Rapid cooling of large igneous bodies can lead to 50% trapped magma in the cumulate pile (Tegner et al., 2009). High degrees of noble gas incompatibility within lower pressure mantle environments, combined with the likely large amount of trapped liquids within magma ocean cumulate piles, implies that the initial noble gas budget of the uppermost mantle was determined by the amount of trapped melt within the cumulate pile. The major source of uncertainty regarding the partitioning of noble gases during magma ocean crystallization relates to their behavior under higher pressures within the mantle.

No direct partitioning studies of noble gases have been completed at the pressures applicable to the deepest magma oceans, but partitioning behavior can be inferred from the solubility ratio of noble gases in the applicable phases at high pressure, namely ultramafic liquid, ferropericlase (FP), and bridgmanite (Brg). Several studies have reported Ar contents of quenched ultramafic liquids (QUL) that were reacted within Ar pressure media using laser-heated diamond anvils cells (LH-DAC) (Chamorro-Perez et al., 1998; Bouhifd and Jephcoat, 2006) (we use the term QUL because molten silicate often quenches to nanometer scale crystals with small amounts of Fe alloy in LH-DAC experiments, Supplementary Fig. 1 and 2). These studies uniformly conclude that Ar solubility in ultramafic liquids plateaus at a concentration of 0.2 wt.% near 5 GPa but sharply decreases to low values (<0.03 wt.%) under higher pressures ($\sim$10 GPa). Higher pressure crystallization of magma oceans is dominated by Brg, and more recent experiments suggest that Ar solubility in Brg may be relatively high, ranging up to 1 wt.% Ar (Shcheka and Keppler, 2012). The reported high Ar solubility in Brg is suggested to reflect abundant, large radius oxygen vacancies that can host also large radius, neutrally charged noble gases.

The combination of high Ar solubility in Brg and low solubility in ultramafic liquid implies Ar, and potentially other neutral species, would be compatible during crystallization of deep magma oceans. A ratio of reported Ar solubility for Brg and ultramafic liquid implies $D^{Ar}_{Brg-melt} \sim 30$. If true, crystallization of Brg from a magma ocean would create a relatively Ar-rich lower mantle. Similarly, fractionation of Brg from a basal magma ocean would create a lowermost mantle that is highly depleted in Ar and potentially other neutral species.

The conclusion of low Ar solubility in ultramafic liquid under high pressures, however, has been challenged. First, the physical mechanism behind the sharp decrease in solubility has remained elusive (Guillot and Sator, 2012). It is expected that noble gases dissolve into larger atomic-scale voids in silicate melts and minerals (Carroll and Stolper, 1993; Jackson et al., 2015). Compression of silicate liquid should decrease the size of atomic-scale voids and therefore may limit noble gas solubility. However, densification of melt is a complex, continuous process (Lee, 2011; Solomatova and Caracas, 2019) and this continuity makes the sharpness of the solubility drop difficult to reconcile with only the effects of compression. Moreover, collapse of He solubility in ultramafic liquids has been reported at the same pressure reported for Ar (Bouhifd et al., 2013). Drops in He solubility related to the compression of silicate liquid should presumably occur at higher pressure relative to Ar given their relative atomic radii. Furthermore, separate experiments aimed at measuring Ar solubility in SiO_2 liquid at high-pressure (up to 19 GPa) failed to reproduce the discontinuous solubility drop. Rather, Ar concentration of quenched SiO_2 liquid remains high beyond the pressures where the solubility drop had previously been reported for this liquid composition (Niwa et al., 2013). The conclusion of high Ar solubility in Brg also remains unverified, leaving the partitioning of Ar, and other neutral species, uncertain in deep magma ocean environments.

We report two parallel series of experiments to constrain the Ar partitioning during deep magma ocean crystallization. The first series comprises Brg, FP, and stishovite (Stv) synthesized in the presence of an Ar-rich fluid using a multi-anvil (MA) press (Fig. 1 and Supplementary Fig. 1). Composition is systemically varied in the MA series to quantify the effect of oxygen vacancies promoting Ar solubility. The second series comprises QUL, Brg, and FP synthesized in the presence of an Ar-rich fluid using a LH-DAC (Fig. 2, Supplementary Figs. 2 and 3). Together, our experiments demonstrate that, up to 100 GPa and 5000 K, Ar solubility in ultramafic liquid remains relatively high ($\sim$1.5 wt.%), whereas Ar solubility in high pressure mineral phases remains relatively low (<0.015 wt.%) despite variations in oxygen vacancy concentrations. Both of these results contrast with previous reports of Ar solubility in high-pressure materials (Chamorro-Perez et al., 1998; Bouhifd and Jephcoat, 2006; Shcheka and Keppler, 2012), and together our new results imply that Ar is highly incompatible ($D^{Ar}_{min-melt} < 0.01$) during deep magma ocean crystallization. We suggest that the initial distribution of Ar, and potentially other highly volatile elements, within the silicate Earth was controlled by liquids trapped during magma ocean crystallization.

2. Methods

2.1. Experimental approach

We conducted a series of experiments using a MA press (Table 1) with the goal of reacting Brg of varying chemistry and point defect populations with Ar-rich fluid. The large volume of MA experiments also enabled analysis by laser-ablation to complement electron microprobe analyses in this subset of our experiments, as detailed below. We also conducted experiments with LH-DACs to document the reactivity of Ar with silicate liquid, Brg, and FP up to *P-T* conditions that approach the core-mantle boundary (Table 1).

Experimental and sample preparation methods for the LH-DAC experiments follow those reported in Jackson et al. (2018) and also are provided in the Supplementary Information. Major element partitioning between metal and QUL confirms reported *P-T* conditions for LH-DAC experiments (Supplementary Fig. 4). We introduced Ar into LH-DAC experiments using a gas-loading device. MA experiments were conducted using 8/3 octahedra, and temperatures were determined by power-temperature curves established for our assembly (Supplementary Fig. 5). Argon was introduced into MA experiments using Ar-bearing glasses as the starting mate-
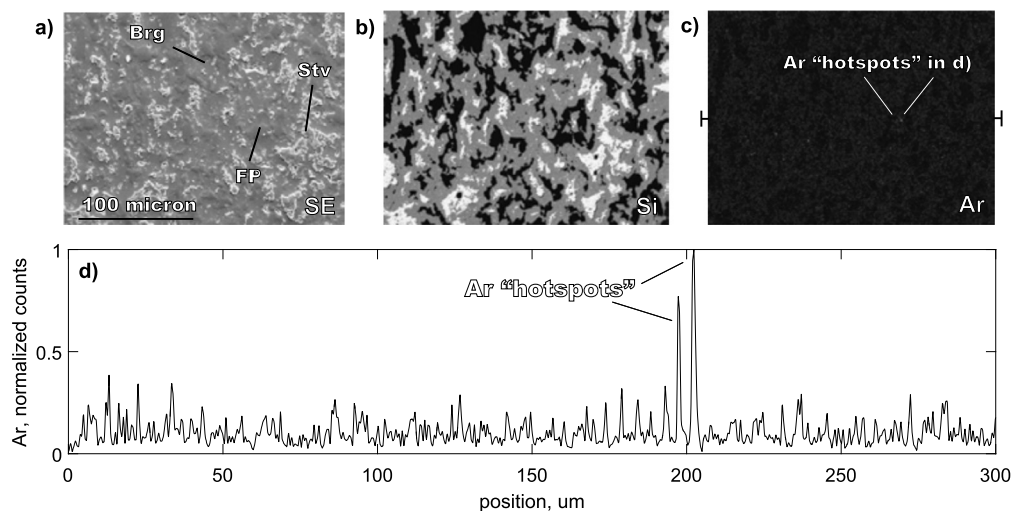
Fig. 1. Representative images of MA experiments (MA_NG_EXP4). **a)** Secondary electron image showing texture of polished surfaces. Stishovite is high relief and Brg is low relief. **b)** Distribution of Si (EDS with focused 10 kV beam) highlights distribution and size of FP, stishovite, and Brg. **c)** Argon map shows distribution of micron-scale, Ar-rich "hotspots" in sample and the relative lack of Ar beyond hotspots. **d)** Horizontal transect across Ar map that intersects pair of Ar hotspots. Location of transect is given by pair of black markers on c).

rials sealed within Pt capsules (Supplementary Table 1). Additional details on MA experimental methods are also reported in the Supplementary Information.

2.2. Chemical analysis

2.2.1. Electron beam microanalysis

Wavelength dispersive spectroscopy (WDS) chemical analyses were completed using a JEOL 8530F field-emission microprobe at the Carnegie Institution for Science, Washington DC. Beam conditions were 10 kV and 1–10 nA. Materials analyzed by WDS in LH-DAC experiments include QUL (Supplementary Table 2), Brg (Supplementary Table 3), and FP (Supplementary Table 4), and Fe–Ni–C alloy (Supplementary Table 5). Analyses on LH-DAC samples used an electron beam that ranged in diameter between focused and 2 μm. Analyses on MA experiments used a 10 μm diameter electron beam. Materials analyzed by WDS in MA experiments include Brg, FP, and Stv (Supplementary Table 6). Our approach to standardizing for Ar analysis is detailed in the Supplementary Information.

2.2.2. Gas-source mass spectrometry chemical analysis

We conducted laser-ablation analyses of MA run products to provide an independent determination of Ar concentrations in our experiments. Samples were ablated under ultra-high vacuum using a 193 nm excimer laser-ablation system connected to a noble gas mass spectrometer in the UC Davis Noble Gas Laboratory. Released gases were gettered prior to trapping Ar on a cryogenic cold finger. Argon was released into the mass spectrometer and analyzed in multi-collection mode. Initial blanks were measured periodically and were relatively high following some sample analyses. In response, we measured blanks bracketing sample analyses for remaining data points. Blank measurements were typically less than 15% (2–3 mV on ^{40}Ar) of the measured sample ^{40}Ar. Further details of this analytical approach are provided in the supplement, and laser-ablation data are reported in Supplementary Table 7.

3. Results

3.1. Multi-anvil series: run product description

MA experiments were completed at 23–24 GPa and 2173–2373 K. Run products were dominated by Brg but contained lesser amounts of FP and Stv. Run products were spatially organized into regions of different mineral assemblages (Fig. 1, Supplementary Fig. 1), likely related to the initial distribution of chemical components (e.g., Ar-bearing SiO_2 glass or MgO) in the starting composition. Regions include pure mineral types but also Brg with either intergrown Stv or FP (Supplementary Fig. 1). Stv and FP cannot coexist at equilibrium, and this is manifested in our experiments by regions with Stv being physically separated from regions with FP. Global disequilibrium, however, does not preclude local equilibrium being established between Ar-bearing fluids and minerals as suggested by the consistency of Ar concentration measurements across experiments (detailed below).

The growth of intergrowing phases appears pinned to a small diameter (∼1 μm). The grain size of majority minerals in a region typically varies between 1–10 μm in diameter. WDS analyses of individual locations of MA experiments are reported in Supplementary Table 6. Small (<1 μm) Ar-rich "hotspots" are observed throughout MA run products.

3.2. LH-DAC series: run product description

LH-DAC experiments with MgO pressure media and a C1/C starting composition (Thibault and Walter, 1995) comprise QUL and quenched Fe–Ni–C alloy liquid mantled by regions of FP and Brg (Fig. 2, Supplementary Fig. 2). The C1/C composition approximates bulk Earth chemistry. These experiments were all run below 57 GPa. FIB-recovery of laser-heated spots reveals FP occurs in direct contact with the QUL. Brg tends to be located several microns away from the QUL. Grains of FP range up to several microns in diameter and are larger grained compared to Brg. The Ar concentrations of the quenched alloy are not reported here and will be the subject of separate manuscript.

LH-DAC experiments with pyrolitic glass pressure media were conducted above 57 GPa. Here FIB-recovery of heating spots reveals QUL mantled by regions of both FP and Brg. FP regions are small (∼1 μm) compared to the MgO pressure media experiments but also occur in direct contact with the QUL (Supplementary Fig. 3). The small size of the FP regions precludes their analysis by WDS. Brg regions occur in direct contact with QUL. Submicron spheres of Fe metal are ubiquitous (bright dots in Supplementary Figs. 2 and 3) despite the starting material only containing oxidized Fe. Possible formation mechanisms include reduction by carbon or disproportionation reactions at pressure (e.g., Frost et
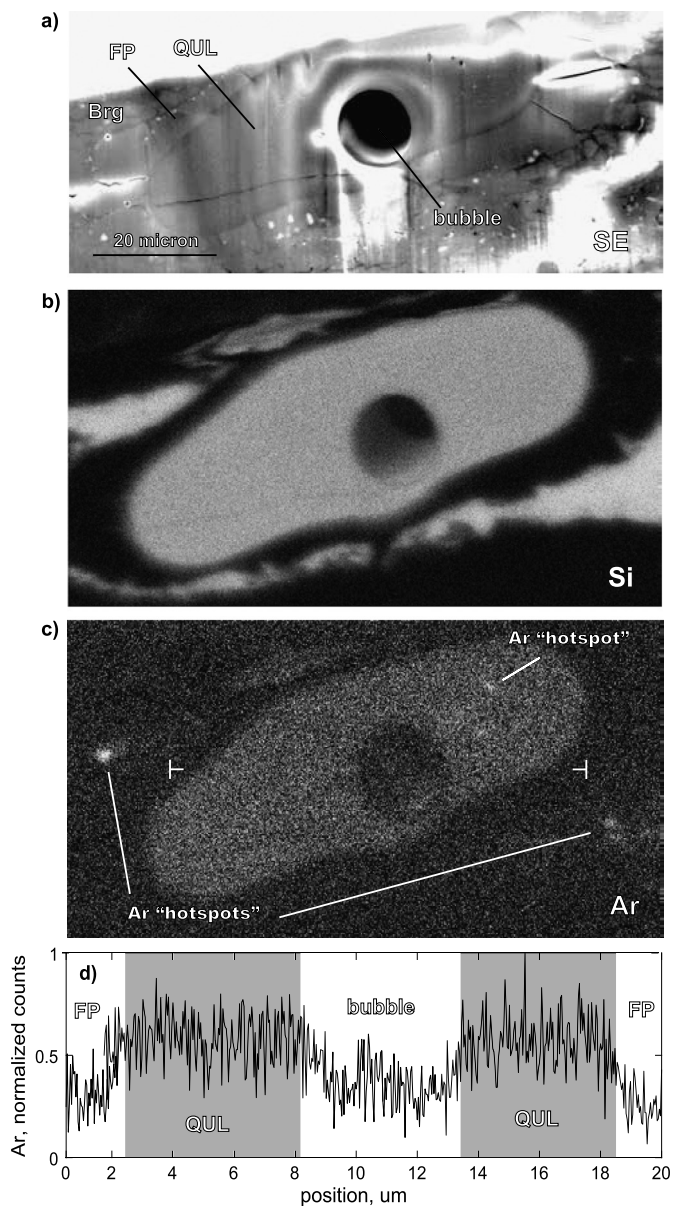
Fig. 2. Representative images of LH_DAC experiments (DAC_NG_EXP28). **a)** Secondary electron image showing texture surfaces prepared by focus ion beam milling. Note that charging can be significant on freshly milled surfaces and leads to locally bright regions. A large bubble is present in the center of the QUL region. **b)** Distribution of Si (EDS with focused 10 kV beam) highlights distribution Si-rich QUL that is surrounded by FP. Brg surrounds the FP region. **c)** Argon map shows uniform distribution of Ar in QUL along with Ar-rich "hotspots" primarily in the Brg region. **d)** Horizontal transect across Ar map that intersects bubble in QUL. Location of transect is given by pair of white markers on c). This heated spot was further milled to expose a quenched metallic sphere contained within the QUL.

al., 2004). EDS mapping of LH-DAC heating spots indicates the presence of small (<1 μm) Ar-rich "hotspots", similar to those observed in MA experiments, particularly in regions rich in Brg (Fig. 2).

3.3. Monitoring of Ar volatilization during WDS analysis

Argon, as a volatile element, is prone to volatilization during electron microprobe analysis, and this behavior may bias Ar measurements to low values. We employed three tests on the different phases explored here to quantify the potential effect of Ar volatilization. First, we analyzed the same region with repeat analyses. Second, we conducted analyses on the same material (differ-

ing locations) with variable beam currents. Third, we measured the Ar count rate as a function of time with the electron beam held in a fixed position on Brg. All tests indicate that Ar is not volatilized under the electron beam conditions employed here (Fig. 3).

3.4. Demonstration of Ar saturation in experiments

EDS mapping of experiments indicates the presence of Ar-rich "hotspots" in the mineral regions of both LH-DAC and MA experiments (Figs. 1 and 2). We interpret these hotspots as trapped Ar inclusions in minerals or in the grain boundaries between minerals. The observation of these Ar-rich regions is key because it indicates the presence of an Ar-rich fluid in the experiments that reflects saturation, but it also provides an explanation for the highly heterogeneous distribution of Ar in the minerals analyzed here. Variable incorporation of Ar-rich fluid inclusions in chemical analyses will generate corresponding variations in Ar concentrations. In LH-DAC experiments, WDS analyses of Ar concentrations in Brg vary from 0.59 wt.% to below detection (<70 ppm), while in MA experiments WDS analyses of Ar in Brg regions vary from 0.14 wt.% to below detection. Laser-ablation analyses of Ar vary from 2.2 wt.% to below detection. We stress that low measured concentrations on minerals are the best estimate of solubility given our observation of Ar-rich inclusions in our experiments.

Evidence for Ar saturation in LH-DAC experiments also comes from experiments conducted at ~30 GPa with variable loading pressures of the Ar pressure medium (Table 1, Supplementary Fig. 5). The objective of this series is to test if Ar solubility was approached in LH-DAC experiments for the Ar loading pressures explored here. Loading pressures within this series varied from 0.01 to 0.1 GPa and are not correlated with Ar concentration in QUL. The lack of correlation between the two parameters indicates that Ar loaded at 0.01 GPa is sufficiently abundant to saturate QUL. Experiments were conducted at temperatures higher than the melting point of Ar (Boehler et al., 2001), allowing Ar to flow from the region surrounding each heating spot to ensure saturation.

X-ray diffraction (XRD) of experiments indicates the presence of solid Ar prior to heating, as further evidence for experiments being conducted under Ar-rich conditions. Ar diffraction peaks are most evident in lower pressure experiments, and in Supplementary Fig. 7 we plot an XRD pattern for DAC_NG_EXP34 spot 1 prior to heating. MgO and Ar are present within unit cell volumes that yield pressures of 15.3 and 13.6 GPa, respectively.

3.5. Distribution of Ar in QUL

EDS mapping and WDS measurements were used to quantify the distribution of Ar within individual QUL samples (Fig. 2, Supplementary Table 2). Both techniques demonstrate a homogeneous distribution of Ar in the large majority of QUL samples on the scale of chemical analysis (~1 μm). It is likely that some crystallization of silicate liquid occurred upon quench (Supplementary Figs. 2 and 4). Given the low solubility of Ar in Brg and FP (below), we expect quench crystallization to bias Ar analyses concentrations to lower than solubility, but this effect may be minimized by barriers to bubble nucleation and loss and/or the trapping of Ar on phase boundaries (Delon et al., 2019). We occasionally observe Ar hotspots in QUL (Fig. 2), and these are interpreted as Ar-rich bubbles trapped below the surface of the QUL. These hotspots are sufficiently rare that they do not inhibit a direct and accurate measurement of Ar solubility in the QUL, in contrast to our measurements of mineral phases.

Many QUL samples contain larger vapor bubbles, but no Ar gradients are observed local to these features (Fig. 2). The large size of the bubbles and the lack of an Ar gradient near the bubble indicate that these are equilibrium features and not formed at quench. The

Table 1
Run conditions.

Series	Experiment	Spot	Location	Starting composition	Ar load P, (GPa)	P, (GPa)	P ±	T, (K)	T ±	Duration (hrs.)	Note
LH-DAC	DAC_NG_EXP26	spot 1	GL	C1/C	0.015	32.0	2.0	2900	NA	NA	pressure by Raman
LH-DAC	DAC_NG_EXP27	spot 1	GL	C1/C	0.050	22.0	2.0	3000	NA	NA	pressure by Raman
LH-DAC	DAC_NG_EXP28	spot 1	GL	C1/C	0.050	30.0	2.0	3400	NA	NA	pressure by Raman
LH-DAC	DAC_NG_EXP29	spot 1	GL	C1/C	0.050	28.0	2.0	3200	NA	NA	pressure by Raman
LH-DAC	DAC_NG_EXP34	spot 1	APS	C1/C, FeSi9	0.100	19.9	2.9	3342	157	NA	high Ar std.
LH-DAC	DAC_NG_EXP34	spot 2	APS	C1/C, FeSi9	0.100	22.5	2.9	3493	133	NA	low total
LH-DAC	DAC_NG_EXP34	spot 3	APS	C1/C, FeSi9	0.100	17.0	4.2	2992	395	NA	
LH-DAC	DAC_NG_EXP34	spot 4	APS	C1/C, FeSi9	0.100	12.5	2.1	2250	17	NA	
LH-DAC	DAC_NG_EXP35	spot 1	APS	C1/C, FeSi9	0.100	22.3	3.3	3683	211	NA	high Ar std.
LH-DAC	DAC_NG_EXP35	spot 2 upper	APS	C1/C, FeSi9	0.100	26.6	2.9	3919	138	NA	
LH-DAC	DAC_NG_EXP35	spot 2 lower	APS	C1/C, FeSi9	0.100	21.9	2.5	3032	73	NA	
LH-DAC	DAC_NG_EXP35	spot 3	APS	C1/C, FeSi9	0.100	23.5	2.9	3093	117	NA	
LH-DAC	DAC_NG_EXP36	spot 1	APS	C1/C	0.100	31.8	2.3	3881	34	NA	
LH-DAC	DAC_NG_EXP36	spot 3	APS	C1/C	0.100	35.9	2.3	4076	33	NA	NiO variations
LH-DAC	DAC_NG_EXP45	spot 1	APS	C1/C	0.010	39.0	2.8	4359	86	NA	
LH-DAC	DAC_NG_EXP45	spot 2	APS	C1/C	0.010	43.8	2.4	4627	45	NA	
LH-DAC	DAC_NG_EXP46	spot 2	APS	C1/C	0.010	35.7	3.0	3882	106	NA	
LH-DAC	DAC_NG_EXP47	spot 1	APS	C1/C	0.010	39.4	2.3	4441	39	NA	high Ar std.
LH-DAC	DAC_NG_EXP47	spot 2	APS	C1/C	0.010	41.6	3.1	4539	115	NA	
LH-DAC	DAC_NG_EXP47	spot 3	APS	C1/C	0.010	41.7	3.0	4559	109	NA	
LH-DAC	DAC_NG_EXP51	spot 2	APS	C1/C	0.013	48.3	2.8	4783	78	NA	
LH-DAC	DAC_NG_EXP51	spot 4	APS	C1/C	0.013	51.9	2.4	5090	44	NA	
LH-DAC	DAC_NG_EXP52	spot 1	APS	C1/C	0.013	55.2	2.5	5138	44	NA	
LH-DAC	DAC_NG_EXP52	spot 2	APS	C1/C	0.013	48.5	2.2	4639	23	NA	
LH-DAC	DAC_NG_EXP52	spot 3	APS	C1/C	0.013	48.7	2.1	4121	8	NA	
LH-DAC	DAC_NG_EXP53	spot 1	APS	pyrolite glass	0.013	81.5	2.6	5886	41	NA	high Ar std.
LH-DAC	DAC_NG_EXP53	spot 2	APS	pyrolite glass	0.013	75.3	2.2	5029	15	NA	
LH-DAC	DAC_NG_EXP54	spot 1	APS	pyrolite glass	0.013	95.0	3.4	5768	87	NA	
LH-DAC	DAC_NG_EXP54	spot 2	APS	pyrolite glass	0.013	101.1	3.6	6345	98	NA	
LH-DAC	DAC_NG_EXP55	spot 2	APS	C1/C	0.013	56.4	2.4	4145	29	NA	
LH-DAC	DAC_NG_EXP55	spot 3	APS	C1/C	0.013	50.9	2.5	4908	50	NA	low total
MA	MA-NG-EXP3	NA	GL	50:50, glass 17:MgO	NA	24	2.0	2173	100	0.75	
MA	MA-NG-EXP4	NA	GL	50:50, glass 17:MgO	NA	23	2.0	2173	100	1.5	
MA	MA-NG-EXP5	NA	GL	75:25, glass 18:MgO	NA	23	2.0	2373	100	1	
MA	MA-NG-EXP6	NA	GL	50:20:20:10, glass 17:glass 18:MgO:Al$_2$O$_3$	NA	24	2.0	2373	100	1.5	
MA	MA-NG-EXP7	NA	GL	50:25:25, glass 17:MgO: FeO-bearing glass	NA	24	2.0	2173	100	1.5	
MA	MA-NG-EXP8	NA	GL	50:50, glass 17:MgO	NA	24	2.0	2173	100	2	

NA = Not applicable; C1/C: Thibault and Walter (1995), pyrolite, glass 17, glass 18 composition reported in Supplementary Table 1.

fact that Ar is homogeneously distributed within individual QUL with >1 wt.% and that many samples have Ar concentrations near 1 wt.% suggests that this concentration is at or near the solubility of Ar under the *P-T* conditions explored. Note that the fluid phase likely contains variable amounts of C or other impurities, diluting the activity of Ar, given that the quenched Fe–Ni–C alloy contains significant C (Supplementary Table 5).

3.6. Distribution of Ar in bridgmanite

EDS mapping and WDS spot measurements were used to quantify the distribution of Ar in regions of Brg and FP in all experiments (Figs. 1 and 2, Supplementary Tables 3, 4 and 6). Laser-ablation mass spectrometry was also used to quantify the distribution of Ar in MA experiments (Supplementary Table 7). Fig. 4 compares Ar analyses by WDS and laser-ablation. Both techniques yield similar results; Ar is heterogeneously distributed, with concentrations ranging from several tenths of a wt.% to below detection. Consistent results between WDS and laser-ablation analyses of MA experiments provides confidence that the distribution of Ar in MA experiments has been properly determined and justifies the use of EPMA to determine Ar concentrations in LH-DAC experiments, which require the high spatial resolution of this technique.

We also note that there is no correlation between the depth of the laser-ablation pit and Ar concentration within Brg (Supplementary Table 7). The lack of correlation with depth demonstrates that Ar dissolved into Brg was not lost from the sample surface

following the polishing procedure and that the measured Ar contents are representative of those present within Brg at elevated *P-T* conditions.

4. Discussion

4.1. Argon incorporation in high-pressure minerals

#### 4.1.1. Oxygen vacancies in bridgmanite

Atomic-scale porosity facilitates noble gas dissolution into minerals and melts (Carroll and Stolper, 1993; Jackson et al., 2015). Porosity can take the form of an interstitial space or vacancy, and because of the large size of noble gases, larger radii interstices or vacancies, such as oxygen vacancies or ring sites, are expected to promote noble gas solubility (Shcheka and Keppler, 2012; Jackson et al., 2015). Brg can contain a relatively high concentration of oxygen vacancies, depending on its composition and the activity of FP (*a*FP) and Al$_2$O$_3$ (Brodholt, 2000; Navrotsky et al., 2003). This crystal chemical behavior has been cited in support of previous reports of high Ar solubility in Brg (Shcheka and Keppler, 2012). The most energetically favorable reactions for producing oxygen vacancies ($V_{\ddot{O}}$) in Brg (ABO$_3$) are (Richmond and Brodholt, 1998):

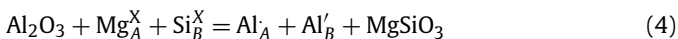$$Al_2O_3 + 2Si_B^X + O_O^X = 2Al_B' + V_{\ddot{O}} + 2SiO_2 \qquad (1)$$
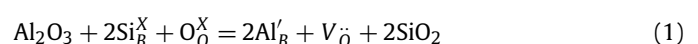
and
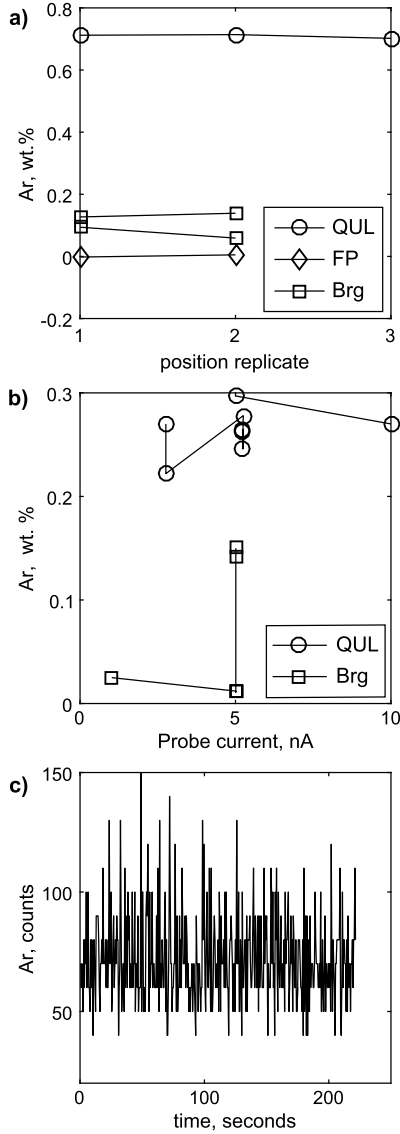
Fig. 3. Replicate Ar analyses of Brg, FP, and QUL to evaluate potential Ar loss during WDS analysis. **a)** Replicate analysis materials at same position. No obvious Ar loss is observed during reanalysis. **b)** Analyses of different locations of materials with varying beam currents. Low current analyses do not systematically yield higher Ar concentrations. **c)** Measurement of count rate as a function of time on Brg. Count rates do not trend with time, and rapid Ar loss near time zero is not observed.

$$Si_B^X + 2O_O^X = V_B'''' + 2V_{\ddot{O}} + SiO_2 \tag{2}$$
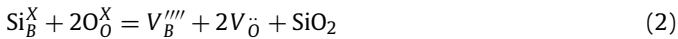
The activity of SiO_2 ($aSiO_2$) will be minimized, and $V_{\ddot{O}}$ maximized, in the lower mantle where FP is present. Alumina is also incorporated into Brg coupled with Fe^{3+} according to the reaction:

$$(Fe, Al)_2O_3 + Mg_A^X + Si_B^X = Fe_A^{\cdot} + Al_B' + MgSiO_3 \tag{3}$$
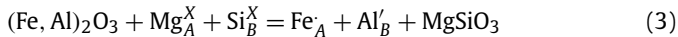
Alumina can also enter into Brg by substituting for Mg and Si:

$$Al_2O_3 + Mg_A^X + Si_B^X = Al_A^{\cdot} + Al_B' + MgSiO_3 \tag{4}$$

Subscripted A and B refer sites within ABO3, while superscripted x, ·, and ′ refer to neutral, positive, and negative charge imbalance for the given occupant, respectively.

Calculations indicate the incorporation of alumina into Brg via Reaction (4) is favored over Reaction (1) with pressure (Richmond and Brodholt, 1998; Brodholt, 2000). Because Fe enables the incorporation of Al without the production of $V_{\ddot{O}}$, Fe-bearing systems should contain Brg with a relatively low $V_{\ddot{O}}$ concentration. In this
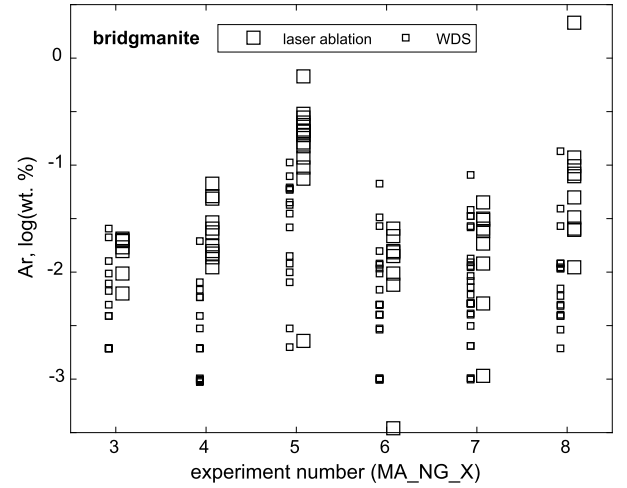
Fig. 4. Comparison of laser-ablation and WDS analyses of Ar concentrations in Brg from MA experiments. Both analytical techniques reveal highly heterogeneous Ar concentrations in all experiments that range from >0.1 to <0.01 wt.%.

context, we conducted Ar solubility experiments across a range of Al contents, Fe contents, $aSiO_2$ values, and pressures to test if $V_{\ddot{O}}$ host significant Ar in Brg.

There are no obvious differences in the distribution of Ar between MA experiments with varying composition analyzed by WDS (Fig. 5). We consistently observe Ar concentrations below detection across MA experiments with compositional variations. Similarly, we do not observe any systematic offset of laser-ablation analyses of Brg and spots that contained Brg+FP (Supplementary Fig. 8). This precludes a determination of the specific role of $V_{\ddot{O}}$ in promoting Ar solubility in Brg, but we can conclude that $V_{\ddot{O}}$ do not lead to a large Ar solubility in Brg (>0.015 wt.%).

4.1.2. Argon solubility limits in bridgmanite: multi-anvil series

Previous work on Ar solubility suggested that up to ∼1 wt.% of Ar could dissolve into Brg (Shcheka and Keppler, 2012). Our present work does not support such a high solubility. Although individual measurements of Ar in Brg from MA series experiments do exceed 1 wt.% (Supplementary Tables 6 and 7), these high values are not constant across all analyses from both laser-ablation and WDS techniques. Such locally high and variable Ar concentrations are inconsistent with a solubility measurement. Rather, highly variable Ar concentrations are consistent with variable incorporation of Ar-rich fluid inclusions, as documented by EDS mapping (Fig. 1). Previous Ar solubility experiments for Brg also reported highly variable Ar concentrations (Shcheka and Keppler, 2012), but these variations were averaged to estimate Ar solubility. Thus, a major difference between the present and previous determinations of Ar solubility in Brg relates to the interpretation, and potentially the magnitude, of Ar variability within experiments.

We take the 25% quartile value of all laser analyses as our best estimate of Ar solubility within MA experiments. This value is 0.015 wt.% Ar (150 ppm). Determining Ar solubility in Brg is complicated by variation in laser-ablation and WDS analyses in single experiments. Analyses that do not sample Ar-rich hotspots should yield the most reliable measurement of solubility. Laser-ablation analyses on Brg in all MA experiments yield at least one measurement below 150 ppm Ar. Similarly, WDS analyses on Brg in all MA experiments yield values below the Ar detection limit (70 ppm). Taken together, 150 ppm is a conservative upper limit on Ar solubility given the MA dataset.

### 4.1.3. Argon solubility limits in bridgmanite: LH-DAC series

Argon analyses of Brg from the LH-DAC series were completed to quantify the *P-T* effects on Ar solubility (Fig. 6). Deep magma
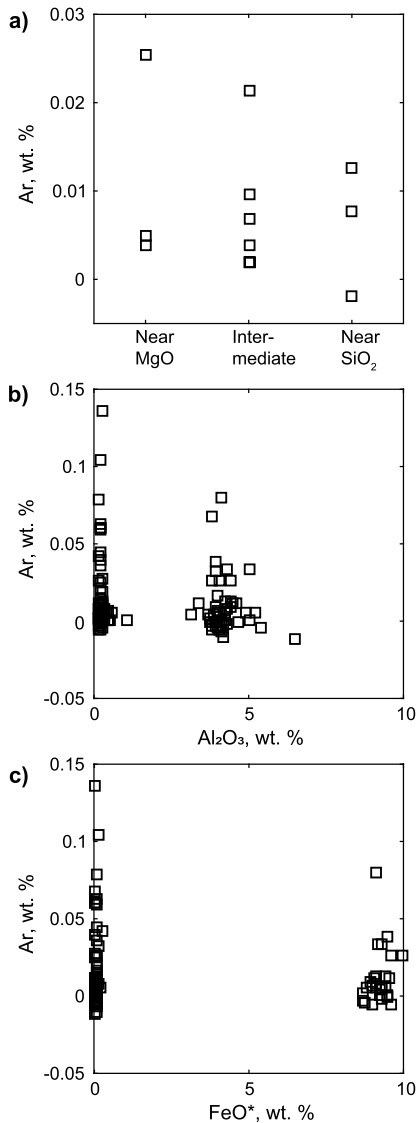
Fig. 5. Argon distribution between Brg with different point defects and major element compositions. **a)** Argon concentration in Brg proximal (~10 μm) to different minerals in MA_NG_EXP4. Brg saturated in MgO should have an elevated concentration of oxygen vacancies, while Brg saturated in SiO_2 should have depressed concentration of oxygen vacancies (Reaction (2)). Argon concentrations are uniformly low in Brg regardless of location. **b)** Argon concentrations in Brg with variable Al_2O_3. The dissolution of Al_2O_3 into Brg can produce oxygen vacancies (Reaction (1)), but no correlation is observed between Al_2O_3 and Ar concentration. **c)** Argon concentrations in Brg with variable FeO*. The incorporation of Fe into Brg should limit the production of oxygen vacancies, but the distribution of Ar concentration measurements is similar between Brg despite variable FeO*.

oceans equilibrate minerals and ultramafic liquid under more extreme *P-T* conditions than those studied in the MA series. Pressure may facilitate dissolution of Ar into minerals due to the highly compressible nature of Ar fluid (Ross et al., 1986), and temperature may facilitate dissolution of Ar into minerals due to entropy favoring the production of vacancies in minerals.

Bridgmanite is stabilized in the regions surrounding QUL, and electron microprobe analyses of these regions yielded Ar concentrations ranging from 0.57 wt.% to below the detection limit (70 ppm) (Fig. 6). Similar to the MA series, hotspots of Ar were identified by EDS mapping of LH-DAC experiments (Fig. 2), and we interpret Ar variability within Brg of LH-DAC experiments as the variable incorporation of hotspot regions in WDS analyses (Supplementary Table 3). Crucially, many WDS analyses of Ar yield undetectable amounts of Ar up to the most extreme *P-T* condi-
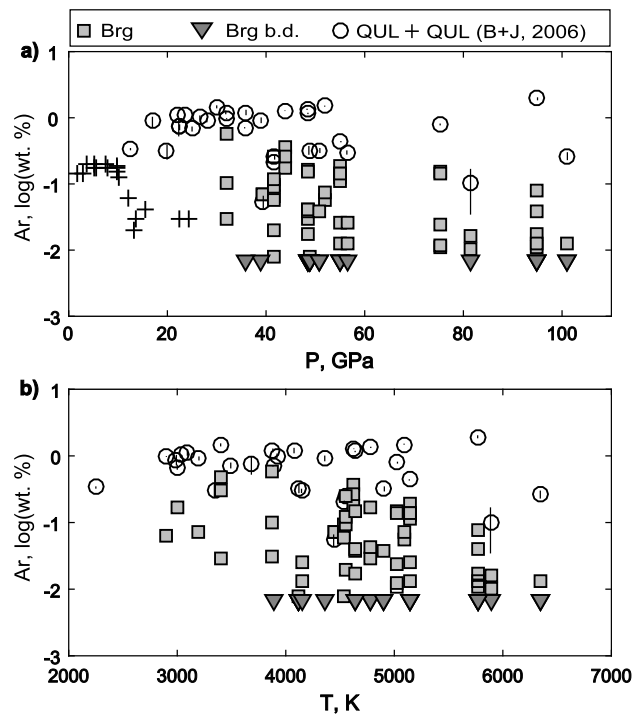
Fig. 6. Argon concentration measurements on QUL (circles) and Brg (squares) plotted as a function of **a)** pressure and **b)** temperature. QUL data points are the average of repeat measurements of individual experiments. Vertical lines associated QUL data points are one standard deviation of the mean. Brg data points are individual measurements of experiments and analyses yielding Ar concentrations below detection are plotted as down-pointing triangles. A subset of Ar analyses on Brg remains below detection, while QUL analyses extend above 1 wt.%, across the range of *P-T* conditions explored.

tions explored here. We conclude that Ar solubility remains low (<150 ppm) in Brg up to 100 GPa and 5000 K. This finding additionally calls into question if Brg can be a significant host for other neutral species in the lower mantle.

4.1.4. Argon solubility limits in ferropericlase

Ferropericlase (FP) constitutes ~20% of the lower mantle and is likely the second phase to crystallize from magma oceans under lower mantle conditions. For these reasons FP may significantly contribute to the budget of Ar and other noble gases in the solid Earth during accretion (Rosa et al., 2020). Ferropericlase was stabilized in both the MA and LH-DAC experiments. Laser-ablation analyses of Ar in FP ranged between 0.28 wt.% to below detection within the MA series (Supplementary Tables 6 and 7, Supplementary Fig. 8). WDS analyses ranged between 0.013 wt.% to below detection for the MA series (Supplementary Table 6) and between 0.15 wt.% to below detection for the LH-DAC series (Fig. 7, Supplementary Table 6). We attribute Ar variability to the incorporation of Ar-rich hotspots, following from our interpretation of Ar concentration measurements in Brg, and we conclude that Ar solubility is sufficiently low in FP that it does not represent a significant reservoir during magma ocean crystallization (c.f., Rosa et al., 2020). A conservative upper limit for the solubility of Ar in the FP is 0.01 wt.%, taking the 25th percentile based on laser-ablation analyses.

4.1.5. Argon solubility limits in stishovite

Stishovite was observed in several MA series of experiments due to incomplete reaction between starting glass (SiO_2-rich, Supplementary Table 1) and MgO. However, the measured Ar concentrations in the mineral should represent the Ar solubility in Stv under Ar saturation considering the high mobility of Ar fluid in the sample chamber. Although stishovite is not expected to crys-
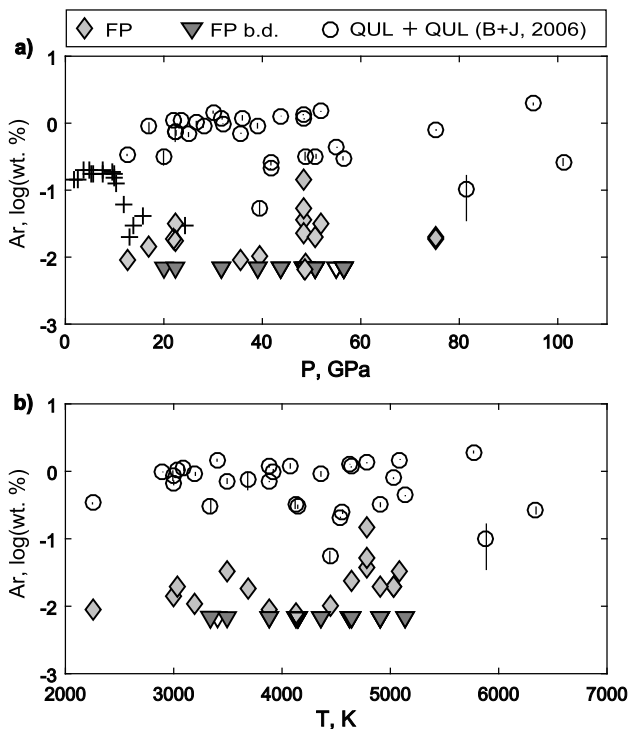
Fig. 7. Argon concentration measurements on QUL (circle) and FP (diamonds) plotted as a function of **a)** pressure and **b)** temperature. QUL data points are the average of repeat measurements of individual experiments. Vertical lines associated with QUL data points are one standard deviation of the mean. FP data points are individual measurements of experiments and analyses yielding Ar concentrations below detection are plotted as down-pointing triangles. A subset of Ar analyses on FP remains below detection, while QUL analyses extend above 1 wt.%, across the range of *P-T* conditions explored.

tallize in magma oceans, it is expected to be present in lower mantle regions rich in recycled oceanic crust. Laser-ablation and WDS analyses of stishovite were collectively highly variable and ranged between 0.77 wt.% to below detection (Supplementary Tables 6 and 7, Supplementary Fig. 8). Argon solubility in stishovite does not appear large when compared to silicate liquids under similar *P-T* conditions. The upper limit solubility of Ar in stishovite is 0.02 wt.%, taking the 25th percentile based on laser-ablation analyses.

4.2. Solubility of Ar in ultramafic liquid

Argon concentrations are consistently near or above 1 wt.% over the range of *P-T* conditions explored (Figs. 6 and 7). The two highest Ar concentrations measured in QUL are 1.499 ± 0.027 and 1.937 ± 0.101 wt.% (Supplementary Table 2). These experiments (DAC_NG_EXP51 spot 4 and DAC_NG_EXP54 spot 1) were conducted over a wide range of pressure (51.9 and 95 GPa) and temperature (5090 and 5768 K). Taken together, these experiments suggest that Ar solubility in ultramafic liquid is at least 1.5 wt.% over much of the *P-T* conditions applicable to Brg and FP crystallization from a magma ocean. We define Ar solubility as the concentration of Ar measured in QUL that was synthesized in the presence of pure Ar fluid. Additional evidence for Ar solubility being ~1 wt.% comes from 1) the homogeneity of Ar within individual QUL samples with ~1 wt.% (Fig. 2, Supplementary Table 2), 2) bubbles present within QUL samples with ~1 wt.% Ar (Fig. 2), and 3) the large number of samples with ~1 wt.% Ar across the investigated *P-T* conditions (Supplementary Table 2).

Solubility of Ar, and other neutral species, in silicate liquid at high pressure reflects the competition between compression of Ar and compression of the liquid. Argon dissolves into large atomic-scale cavities within silicate liquids (Carroll and Stolper, 1993), and

the production of large cavities becomes increasingly entropically and volumetrically punitive at higher pressures (Guillot and Sator, 2012). At the same time, the size of Ar progressively diminishes with pressure, allowing Ar to dissolve into smaller cavities (Ross et al., 1986). The nearly constant solubility observed for Ar up to 100 GPa suggests the effects of Ar compaction, the energy cost of cavity formation, and the increased experimental temperatures with pressure largely counter each other.

Our results contrast previous studies that observed a sharp drop in Ar solubility within ultramafic liquid with increasing pressure (Chamorro-Perez et al., 1998; Bouhifd and Jephcoat, 2006). The root cause of this discrepancy is not certain, but we note that previous works used a CO_2 laser for heating or scanned a diode-pumped laser laser over the sample chamber (Chamorro-Perez et al., 1998; Bouhifd and Jephcoat, 2006). Our approach is to heat a single area with a diode-pumped laser. We suggest our approach enables relatively rapid quenching and a greater propensity to retain Ar.

4.3. Argon partitioning within magma ocean environments

The partitioning of any element can be inferred by the ratio of its solubility in two phases that are in equilibrium with each other (Fig. 6 and 7). This study seeks to constrain the partitioning of Ar within deep magma ocean environments by measuring its solubility in the applicable phases (Brg, ultramafic liquid, and FP) across the applicable *P-T* conditions (up to 5000 K and 100 GPa). The solubility results reported here indicate that Ar is at least ~100× more soluble in ultramafic liquid (1.5 wt.%), compared to Brg or FP (0.015 wt. or 0.01 wt.%, respectively) under *P-T* conditions applicable to deep magma oceans and high fAr. This yields values for $D^{Ar}_{Brg-melt}$ and $D^{Ar}_{FP-melt}$ of 0.01 as conservative upper estimates.

Previous work completed at lower pressures also demonstrates that Ar is highly incompatible in upper mantle (lower pressure) minerals (Chamorro et al., 2002; Brooker et al., 2003; Heber et al., 2007; Jackson et al., 2013). Two LH-DAC experiments stabilized a $(Mg,Fe)_2SiO_4$ stoichiometry phase (DAC_NG_EXP27 and 34 spot 1) that were subsequently analyzed by WDS. These phases were not systematically analyzed, but two analyses yielded Ar concentrations of 0.17 wt.% and below detection. XRD analysis of DAC_NG_EXP34 spot 1 indicates the presence of ringwoodite, and thus, ringwoodite does also not appear to be a significant host for Ar. Taken together, available experiments imply Ar incompatibility throughout the crystallization sequence of a magma ocean, from deep to shallow.

We stress that the current study quantifies Ar solubility at higher fugacity than is naturally applicable. Extrapolation to very low fAr is required to predict the partitioning behavior of Ar in magma oceans. Given that Ar solubility does not strongly vary for Brg, FP, and ultramafic liquid across the *P-T* conditions explored here, it is likely that Ar solubility is a reflection of the total sites available for Ar to occupy in a given phase. It is not guaranteed, however, that the proportion of sites occupied by Ar in each phase will scale in the same way as fAr decreases. This would be reflected by a shift in Ar partitioning between the experimental and natural conditions.

4.4. Argon trapped in a magma ocean with crystal fractionation

Argon, as an incompatible element, will be primarily contained within the silicate liquid of a magma ocean compared to crystallizing minerals. We take the partitioning of Ar, being the median noble gas in terms of atomic radius, as broadly representative of the noble gas family.

With cooling, magma oceans crystallize and some silicate liquid is trapped in the growing cumulate pile. The amount of
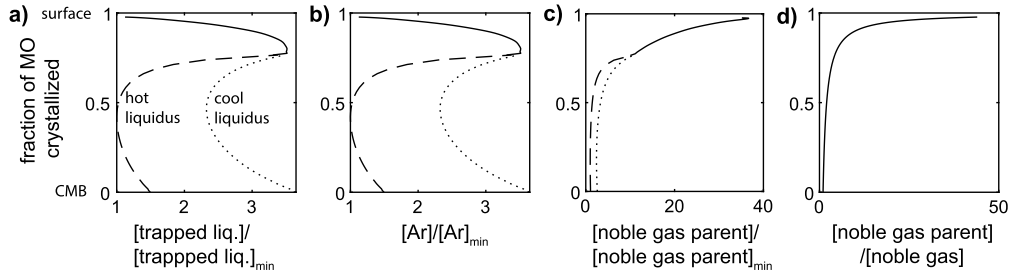
Fig. 8. Models of element trapping in a cumulate pile of a bottom-up crystallizing magma ocean. Crystallization is considered for a whole mantle magma ocean. **a)** Concentration of trapped liquids in the magma ocean cumulate pile normalized to the minimum predicted amount of trapped liquid. The dash line assumes the hotter liquidus of Fiquet et al. (2010), while the dotted line assumes cooler liquidus of Andrault et al. (2011) for calculating ΔT values. Trapped liquid abundances at each depth with the cumulate pile are calculated by solving Eqs. (5) and (6) over the duration of magma ocean crystallization. **b)** Concentration of Ar trapped in cumulates plotted as a function of crystallization progress. We calculate the distribution of Ar assuming that its concentration in the mantle is solely controlled by abundance of liquids trapped in cumulates during magma ocean crystallization. **c)** The abundance trapped noble gas parent elements normalized the minimum calculated value. Perfect incompatibly and no volatility, is assumed for parent elements. **d)** Noble gas parent/daughter ratios increase in trapped liquids as a function of crystallization progress. This increase reflects that noble gases degas from the magma ocean but parent elements remain undegassed.

trapped liquid reflects a competition between freezing and expulsion within the compacting cumulate pile (McKenzie, 1984). Geochemical studies of large igneous intrusions, which are considered small-scale analogs for magma oceans, suggest that trapped liquids can approach 50 mass% of the cumulate pile (Tegner et al., 2009), but even small amounts (∼1%) of trapped liquid are sufficient to control the distribution of incompatible elements like Ar in a crystallizing magma ocean.

Our focus is on the *relative* distribution of trapped liquids in a growing cumulate pile because many parameters that influence the absolute amount of trapped liquid remain poorly defined. These include the compaction timescale, initial cumulate pile porosity, and emissivity of the primordial atmosphere.

We modify the approach outlined in Hier-Majumder and Hirschmann (2017) to calculate relative amounts of trapped liquids ($F_{Tr.Liq.,Rel.}$) in a growing cumulate pile of a magma ocean:

$$F_{Tr.Liq,Rel.} = \frac{(dT/dt)_{Rel.}}{\Delta T} \tag{5}$$

where ΔT is the temperature difference between the liquidus and solidus at the depth where crystallization is occurring and $(dT/dt)_{Rel.}$ is the relative cooling rate of the magma ocean (Supplementary Fig. 9). To calculate the potential range of ΔT values over the duration of crystallization, we first take solidus and liquidus curves from Fiquet et al. (2010) to define ΔT for a hot liquidus. We then take the solidus from Fiquet et al. (2010) and the liquidus from Andrault et al. (2011) to define ΔT for a cool liquidus (Fig. 8a). The relative magma ocean cooling rates are calculated as:

$$(dT/dt)_{Rel.} = -T_p^4 / \left[C_p \left(\frac{R^3 - a^3}{3} \right) - \Delta S_{melt} T_{solidus} a^2 da/dT \right] \tag{6}$$

where T_p is the magma ocean potential temperature, a is the depth of the magma ocean, R is the radius of Earth, C_p is the heat capacity of the magma ocean (1000 J kg^{-1} K^{-1}), ΔS_{melt} is the entropy change upon melting (300 J kg^{-1} K^{-1}), and $T_{solidus}$ is the temperature of crystallization. The depth of the magma ocean for any temperature is approximated as the solidus curve, and values of da/dT are calculated by differentiating the solidus curve. Potential temperature is calculated assuming a constant adiabatic gradient from $T_{solidus}$ of 3×10^{-4} K m^{-1} to the surface. Parameter values are taken from Hier-Majumder and Hirschmann (2017) and references within.

We assume that trapped liquid is the only host of Ar, given its incompatibility in minerals, and that the concentration of Ar in the magma ocean is fixed by continuous exchange with the overlying

primordial atmosphere, i.e. a single Henry's constant describes the concentration of Ar in the magma ocean. Given our assumptions, the relative distribution of Ar in the cumulate layer is solely determined by the distribution of trapped liquids (Fig. 8a). Calculations assume a bottom-up crystallization of whole mantle magma ocean and we normalize predicted Ar concentrations by the minimum predicted concentration. Values calculated for the cool and hot liquidus curves are plotted as dotted and dashed lines that converge to well-established melting relationships at lower *P-T* conditions. A hotter liquidus results in a larger ΔT value with correspondingly slower crystallization and less trapped liquid.

The concentration of Ar trapped in any horizon of the cumulates reflects a competition between $(dT/dt)_{Rel.}$ and ΔT values (Eq. (5)). Values for both parameters are maximized at the onset of crystallization in the lowermost mantle. As crystallization progresses upwards, $(dT/dt)_{Rel.}$ and ΔT decrease from their maximum values, but $(dT/dt)_{Rel.}$ drops proportionally faster (Supplementary Fig. 9), leading to a declining amount of trapped liquid in the mid-mantle and, hence, lower concentrations of Ar. As the magma ocean approaches complete solidification there is a relatively rapid increase in trapped Ar concentrations due to the narrowing of the ΔT interval (Supplementary Fig. 9) resulting in more rapid crystallization and larger amounts of trapped liquid.

Fig. 8b shows that early (first ∼10% crystallized, lower-most mantle) and near-final (70–90% crystallized, upper mantle) cumulates of a whole mantle magma ocean have the highest initial concentrations of Ar. The final cumulates are predicted to be Ar-poor because cooling rates become relatively slow, allowing for more trapped liquid to be expelled from the cumulate pile. It is possible that the cumulate pile overturns in response to an unstable density profile (e.g., Elkins-Tanton, 2012). If this occurs for Earth's magma ocean, this could place the near-final, relatively noble gas-rich cumulates near the core-mantle boundary.

4.5. Noble gas parent (U, Th, K, I and Pu) in trapped liquids of a crystallization magma ocean

The noble gas group of elements contains many isotopes produced by the decay of short- and long-lived radioactive isotopes. Noble gas parent elements, U, Th, K, I and Pu, are likely incompatible in mantle minerals (e.g., Corgne et al., 2005), and similar to the noble gases, their distribution in crystallizing magma oceans may be controlled by trapped liquids. If it is assumed that noble gas parent elements are incompatible and non-volatile, their concentration within trapped liquids will increase as 1/F (F, fraction of magma ocean still liquid) and their concentration in any horizon of the cumulate pile is determined by the product of 1/F and the local abundance of trapped liquid (x-axis, Fig. 8c).

A key process to generating initial variations in noble gas parent-daughter ratios is thus the outgassing of noble gases to the primordial atmosphere but retention of their parent elements in the residual liquid formed response to magma ocean crystallization (Fig. 8d). With this dynamic, parent-daughter ratios of noble gas systems will continue to increase to the final solidification of the magma ocean in the uppermost mantle (x-axis, Fig. 8d). Cumulate overturn, if operable, would then send upper mantle materials, with high noble gas parent-daughter ratios, to the deep mantle. All other things being equal, cumulates with a high noble gas parent-daughter ratios will evolve relatively radiogenic signatures of He, Ne, Ar, and Xe, opposite to the observations of high ^{3}He/^{4}He materials (Jenkins, 1978; Kaneoka and Takaoka, 1980; Kurz et al., 1982; Honda et al., 1991; Farley and Craig, 1994; Burnard et al., 1997; Trieloff et al., 2000; Moreira et al., 2001; Kurz et al., 2009). This analysis, however, neglects subsequent mantle processing, which will lower the parent-daughter ratios of the processed regions (Jackson et al., 2013).

4.6. Accumulation of Ar in a basal magma ocean

It is possible that dense magma accumulated near the core-mantle boundary during Earth's growth to create a basal magma ocean (e.g., Labrosse et al., 2007). Self-compression and Brg fractionation can produce dense magma, or dense magma may alternatively form in response to high *P-T* reaction with core-forming metal (Kaminski and Javoy, 2013; Jackson et al., 2018). A basal magma ocean would crystallize with cooling, but because basal magma ocean liquids do not ascend to shallow depth where degassing can occur, we predict Ar, and likely other noble gases, would accumulate, along with their radioactive parents, following a 1/F relationship given their mutual incompatibility in Brg and FP. The net effect of a basal magma ocean would be to generate a chemically dense reservoir with elevated concentrations of noble gases but not elevated parent-daughter ratios. This is an attractive scenario for the formation of high ^{3}He/^{4}He materials given 1) their low time-integrated parent-daughter ratios (He, Ne, Ar, and Xe isotopic signatures) and 2) the requirement for long-term and early isolation from both Xe and Ne isotopes (Honda et al., 1991; Farley and Craig, 1994; Burnard et al., 1997; Trieloff et al., 2000; Moreira et al., 2001; Kurz et al., 2009; Mukhopadhyay, 2012; Peto et al., 2013; Caracausi et al., 2016; Williams and Mukhopadhyay, 2019). Early-forming, dense materials may now be manifested by regions of low and ultra-low shear velocity in the lowermost mantle (e.g., Garnero and McNamara, 2008).

We note that source regions of high ^{3}He/^{4}He basalts contain ~90% atmospheric Xe (e.g., Mukhopadhyay, 2012; Peto et al., 2013), and therefore the heavy noble gas and lithophile element composition of high ^{3}He/^{4}He mantle is likely dominated by recycled, rather than primitive, materials. Only elements that are little recycled by subduction, such as He and Ne, may retain an observable signature related to the formation of the high ^{3}He/^{4}He source.

5. Conclusions

Two series of high *P-T* experiments indicate that Ar is incompatible during crystallization of deep magma oceans ($D^{Ar}_{bridgmanite-melt} < 0.01$, $D^{Ar}_{ferropericlase-melt} < 0.01$). Our inference of incompatibly is based on upper-limit constraints we derived for Ar solubility in Brg and FP. These results, in combination with literature results (Brooker et al., 2003; Heber et al., 2007; Delon et al., 2019; Jackson et al., 2013), imply that Ar is highly incompatible in all stages of magma ocean crystallization, with the caveat that solubility measurements were conducted under higher *f*Ar than directly applicable. Highly incompatible Ar, and potentially other neutral species, would overwhelmingly reside within the magma

of a magma ocean, and retention in the silicate Earth will be determined by the trapping of liquids in the magma ocean cumulate pile. Trapped liquid modeling for magma ocean environments indicates that the upper mantle may have contained higher initial concentrations of Ar compared to the lower mantle. Radioactive parents of noble gases will concentrate more efficiently in the upper mantle compared to Ar, and likely other noble gases, due to the outgassing of the magma ocean in response to crystallization. These behaviors result in an upper mantle with an elevated noble gas parent-daughter ratio compared to the lower mantle despite overall enrichment in noble gases. Cumulate overturn may mix upper mantle cumulates downward and vice versa. Basal magma oceans will become progressively Ar-rich during fractionation of Brg and FP.

CRediT authorship contribution statement

All authors contributed to the drafting of the manuscript. Jackson performed the experiments, prepared the experiments, completed the microprobe analysis, and completed the first draft of the manuscript. Williams completed the laser-ablation analyses. Fei facilitated the completion of the multi-anvil and LH-DAC experiments. Fei also contributed to the analysis of the XRD data. Mukhopadhyay facilitated the laser-ablation analyses. Du and Bennett contributed to the execution of the experiments. Du and Bennett also helped develop the methods employed for LH-DAC sample recovered and microprobe analysis.

Declaration of competing interest

The authors declare that they have no known competing financial interests or personal relationships that could have appeared to influence the work reported in this paper.

Acknowledgements

Appendix A. Supplementary material

Supplementary material related to this article can be found online at https://doi.org/10.1016/j.epsl.2020.116598.

References

Andrault, D., Bolfan-Casanova, N., Lo Nigro, G., Bouhifd, M.A., Garbarino, G., Mezouar, M., 2011. Solidus and liquidus profiles of chondritic mantle: implication for

melting of the Earth across its history. Earth Planet. Sci. Lett. 304 (1–2), 251–259.

Boehler, R., Ross, M., Söderlind, P., Boercker, D.B., 2001. High-pressure melting curves of argon, krypton, and xenon: deviation from corresponding states theory. Phys. Rev. Lett. 86 (25), 5731.

Bouhifd, M., Jephcoat, A.P., Heber, V.S., Kelley, S.P., 2013. Helium in Earth's early core. Nat. Geosci. 6, 982–986.

Bouhifd, M.A., Jephcoat, A.P., 2006. Aluminium control of argon solubility in silicate melts under pressure. Nature 439 (7079), 961–964.

Brodholt, J.P., 2000. Pressure-induced changes in the compression mechanism of aluminous perovskite in the Earth's mantle. Nature 407 (6804), 620–622.

Brooker, R.A., Du, Z., Blundy, J.D., Kelley, S.P., Allan, N.L., Wood, B.J., Chamorro, E.M., Wartho, J.A., Purton, J.A., 2003. The 'zero charge' partitioning behaviour of noble gases during mantle melting. Nature 423 (6941), 738–741.

Burnard, P., Graham, D., Turner, G., 1997. Vesicle-specific noble gas analyses of "popping rock": implications for primordial noble gases in Earth. Science 276 (5312), 568–571.

Caracausi, A., Avice, G., Burnard, P.G., Füri, E., Marty, B., 2016. Chondritic xenon in the Earth's mantle. Nature 533 (7601), 82–85.

Carroll, M.R., Stolper, E.M., 1993. Noble gas solubilities in silicate melts and glasses: new experimental results for argon and the relationship between solubility and ionic porosity. Geochim. Cosmochim. Acta 57 (23–24), 5039–5051.

Chamorro, E.M., Brooker, R.A., Wartho, J.A., Wood, B.J., Kelley, S.P., Blundy, J.D., 2002. Ar and K partitioning between clinopyroxene and silicate melt to 8 GPa. Geochim. Cosmochim. Acta 66 (3).

Chamorro-Perez, E., Gillet, P., Jambon, A., Badro, J., McMillan, P., 1998. Low argon solubility in silicate melts at high pressure. Nature 393 (6683).

Corgne, A., Liebske, C., Wood, B.J., Rubie, D.C., Frost, D.J., 2005. Silicate perovskite-melt partitioning of trace elements and geochemical signature of a deep perovskitic reservoir. Geochim. Cosmochim. Acta 69 (2), 485–496.

Delon, R., Demouchy, S., Marrocchi, Y., Bouhifd, M.A., Cordier, P., Addad, A., Burnard, P.G., 2019. Argon storage and diffusion in Earth's upper mantle. Geochim. Cosmochim. Acta 253, 1–18.

Elkins-Tanton, L.T., 2012. Magma oceans in the inner solar system. Annu. Rev. Earth Planet. Sci. 40, 113–139.

Farley, K., Craig, H., 1994. Atmospheric argon contamination of ocean island basalt olivine phenocrysts. Geochim. Cosmochim. Acta 58 (11), 2509–2517.

Fiquet, G., Auzende, A.L., Siebert, J., Corgne, A., Bureau, H., Ozawa, H., Garbarino, G., 2010. Melting of peridotite to 140 gigapascals. Science 329 (5998), 1516–1518.

Frost, D.J., Liebske, C., Langenhorst, F., McCammon, C.A., Tronnes, R.G., Rubie, D.C., 2004. Experimental evidence for the existence of iron-rich metal in the Earth's lower mantle. Nature 428 (6981), 409–412.

Garnero, E.J., McNamara, A.K., 2008. Structure and dynamics of Earth's lower mantle. Science 320 (5876), 626–628.

Graham, D.W., Michael, P.J., Shea, T., 2016. Extreme incompatibility of helium during mantle melting: evidence from undegassed mid-ocean ridge basalts. Earth Planet. Sci. Lett. 454, 192–202.

Guillot, B., Sator, N., 2012. Noble gases in high-pressure silicate liquids: a computer simulation study. Geochim. Cosmochim. Acta 80, 51–69.

Heber, V.S., Brooker, R.A., Kelley, S.P., Wood, B.J., 2007. Crystal-melt partitioning of noble gases (helium, neon, argon, krypton, and xenon) for olivine and clinopyroxene. Geochim. Cosmochim. Acta 71 (4), 1041–1061.

Hier-Majumder, S., Hirschmann, M.M., 2017. The origin of volatiles in the Earth's mantle. Geochem. Geophys. Geosyst. 18 (8), 3078–3092.

Honda, M., McDougall, I., Patterson, D.B., Doulgeris, A., Clague, D.A., 1991. Possible solar noble gas component in Hawaiian basalts. Nature 349 (6305), 149–151.

Jackson, C.R.M., Parman, S.W., Kelley, S.P., Cooper, R.F., 2013. Constraints on light noble gas partitioning at the conditions of spinel-peridotite melting. Earth Planet. Sci. Lett. 384, 178–187.

Jackson, C.R.M., Parman, S.W., Kelley, S.P., Cooper, R.F., 2015. Light noble gas dissolution into ring structure-bearing materials and lattice influences on noble gas recycling. Geochim. Cosmochim. Acta 159, 1–15.

Jackson, C.R., Bennett, N.R., Du, Z., Cottrell, E., Fei, Y., 2018. Early episodes of high-pressure core formation preserved in plume mantle. Nature 553 (7689), 491.

Jenkins, W., 1978. Excess ^{3}He and ^{4}He in Galapagos submarine hydrothermal waters. Nature 272, 156–158.

Kaminski, E., Javoy, M., 2013. A two-stage scenario for the formation of the Earth's mantle and core. Earth Planet. Sci. Lett. 365, 97–107.

Kaneoka, I., Takaoka, N., 1980. Rare gas isotopes in Hawaiian ultramafic nodules and volcanic rocks: constraint on genetic relationships. Science 208 (4450), 1366–1368.

Kurz, M.D., Curtice, J., Fornari, D., Geist, D., Moreira, M., 2009. Primitive neon from the center of the Galapagos hotspot. Earth Planet. Sci. Lett. 286 (1–2).

Kurz, M.D., Jenkins, W.J., Hart, S.R., 1982. Helium isotopic systematics of oceanic islands and mantle heterogeneity. Nature 297 (5861), 43–47.

Labrosse, S., Hernlund, J.W., Coltice, N., 2007. A crystallizing dense magma ocean at the base of the Earth's mantle. Nature 450 (7171), 866–869.

Lee, S.K., 2011. Simplicity in melt densification in multicomponent magmatic reservoirs in Earth's interior revealed by multinuclear magnetic resonance. Proc. Natl. Acad. Sci. 108 (17), 6847–6852.

Mamajek, E.E., 2009. Initial conditions of planet formation: lifetimes of primordial disks. In: AIP Conference Proceedings. American Institute of Physics, pp. 3–10.

McKenzie, D., 1984. The generation and compaction of partially molten rock. J. Petrol. 25 (3), 713–765.

Moreira, M., Breddam, K., Curtice, J., Kurz, M.D., 2001. Solar neon in the Icelandic mantle: new evidence for an undegassed lower mantle. Earth Planet. Sci. Lett. 185 (1), 15–23.

Mukhopadhyay, S., 2012. Early differentiation and volatile accretion recorded in deep-mantle neon and xenon. Nature 486 (7401).

Mundl, A., Touboul, M., Jackson, M.G., Day, J.M., Kurz, M.D., Lekic, V., Helz, R.T., Walker, R.J., 2017. Tungsten-182 heterogeneity in modern ocean island basalts. Science 356 (6333), 66–69.

Navrotsky, A., Schoenitz, M., Kojitani, H., Xu, H., Zhang, J., Weidner, D.J., Jeanloz, R., 2003. Aluminum in magnesium silicate perovskite: formation, structure, and energetics of magnesium-rich defect solid solutions. J. Geophys. Res., Solid Earth 108 (B7).

Niwa, K., Miyakawa, C., Yagi, T., Matsuda, J.-i., 2013. Argon solubility in SiO_2 melt under high pressures: a new experimental result using laser-heated diamond anvil cell. Earth Planet. Sci. Lett. 363, 1–8.

Peto, M.K., Mukhopadhyay, S., Kelley, K.A., 2013. Heterogeneities from the first 100 million years recorded in deep mantle noble gases from the Northern Lau Back-arc Basin. Earth Planet. Sci. Lett. 369, 13–23.

Richmond, N.C., Brodholt, J.P., 1998. Calculated role of aluminum in the incorporation of ferric iron into magnesium silicate perovskite. Am. Mineral. 83 (9–10), 947–951.

Rizo, H., Walker, R.J., Carlson, R.W., Horan, M.F., Mukhopadhyay, S., Manthos, V., Francis, D., Jackson, M.G., 2016. Preservation of Earth-forming events in the tungsten isotopic composition of modern flood basalts. Science 352 (6287), 809–812.

Rosa, A., Bouhifd, M.A., Morard, G., Briggs, R., Garbarino, G., Irifune, T., Mathon, O., Pascarelli, S., 2020. Krypton storage capacity of the Earth's lower mantle. Earth Planet. Sci. Lett. 532, 116032.

Ross, M., Mao, H., Bell, P., Xu, J., 1986. The equation of state of dense argon: a comparison of shock and static studies. J. Chem. Phys. 85 (2), 1028–1033.

Shcheka, S.S., Keppler, H., 2012. The origin of the terrestrial noble-gas signature. Nature 490 (7421).

Solomatova, N., Caracas, R., 2019. Pressure-induced coordination changes in a pyrolitic silicate melt from ab initio molecular dynamics simulations. J. Geophys. Res., Solid Earth 124 (11), 11232–11250.

Tegner, C., Thy, P., Holness, M.B., Jakobsen, J.K., Lesher, C.E., 2009. Differentiation and compaction in the Skaergaard intrusion. J. Petrol. 50 (5), 813–840.

Thibault, Y., Walter, M.J., 1995. The influence of pressure and temperature on the metal-silicate partition coefficients of nickel and cobalt in a model C1 chondrite and implications for metal segregation in a deep magma ocean. Geochim. Cosmochim. Acta 59 (5), 991–1002.

Trieloff, M., Kunz, J., Clague, D.A., Harrison, D., Allegre, C.J., 2000. The nature of pristine noble gases in mantle plumes. Science 288 (5468), 1036–1038.

Watson, E.B., Thomas, J.B., Cherniak, D.J., 2007. Ar40 retention in the terrestrial planets. Nature 449 (7160).

Williams, C.D., Mukhopadhyay, S., 2019. Capture of nebular gases during Earth's accretion is preserved in deep-mantle neon. Nature 565 (7737), 78.